

Article

Hydrothermal Synthesis of Three-Dimensional Perovskite NiMnO₃ Oxide and Application in Supercapacitor Electrode

Hyo-Young Kim ¹, Jeeyoung Shin ^{2,3}, Il-Chan Jang ^{4,*}, and Young-Wan Ju ^{1,*}

¹ Department of Chemical Engineering, College of Engineering, Wonkwang University, Iksan, Jeonbuk 54538, Korea

² Department of Mechanical Systems Engineering, Sookmyung Women's University, Seoul 04310, Korea

³ Institute of Advanced Materials and Systems, Sookmyung Women's University, Seoul 04310, Korea

⁴ Gwangju Bio/Energy R&D Center, Korea Institute of Energy Research, Gwangju 61003, Korea

* Correspondence: ywju1978@wku.ac.kr (Y.-W.J.); jic7421@kier.re.kr (I.-C.J.)

Received: 8 November 2019; Accepted: 16 December 2019; Published: 19 December 2019

Abstract: Supercapacitors are attractive as a major energy storage device due to their high coulombic efficiency and semi-permanent life cycle. Transition metal oxides are used as electrode material in supercapacitors due to their high conductivity, capacitance, and multiple oxidation states. Nanopowder transition metal oxides exhibit low specific surface area, ion diffusion, electrical conductivity, and structural stability compared with the three-dimensional (3D) structure. Furthermore, unstable performance during long-term testing can occur via structural transition. Therefore, it is necessary to synthesize a transition metal oxide with a high specific surface area and a stable structure for supercapacitor application. Transition metal oxides with a perovskite structure control structural transition and improve conductivity. In this study, a NiMnO₃ perovskite oxide with a high specific surface area and electrochemical properties was obtained via hydrothermal synthesis at low temperature. Hydrothermal synthesis was used to fabricate materials with an aqueous solution under high temperature and pressure. The shape and composition were regulated by controlling the hydrothermal synthesis reaction temperature and time. The synthesis of NiMnO₃ was controlled by the reaction time to alter the specific surface area and morphology. The prepared perovskite NiMnO₃ oxide with a three-dimensional structure can be used as an active electrode material for supercapacitors and electrochemical catalysts. The prepared NiMnO₃ perovskite oxide showed a high specific capacitance of 99.03 F·g⁻¹ and excellent cycle stability with a coulombic efficiency of 77% even after 7000 cycles.

Keywords: three-dimensional (3D) structure; perovskite; hydrothermal synthesis; Oxygen Reduction Reaction (ORR) catalysts; supercapacitors

1. Introduction

The supercapacitor has attracted substantial interest as an alternative energy storage system due to its high power density, rapid charging/discharging process, and semi-permanent cycle life [1–3]. Supercapacitors can be classified into two types. The first type is an electric double-layered capacitor, which can store electric energy via the formation of an electric double layer at the interface between electrode and electrolyte. The second type is a pseudocapacitor based on the redox reaction of the electrode. In spite of the high power density, issues such as lower energy density still inhibit the widespread application of supercapacitors. Therefore, many research groups have investigated electrode materials that carry high specific surface areas and electrical conductivity for increased energy density [4].

Electrode materials for supercapacitors should store the charge stably without structural transition and exhibit two or more oxidation states and high electroconductivity. Transition metal oxides are suitable due to their multi-oxidation states that enable the charge transfer via oxygen reduction, facilitating multiple-electron transfer and good structural stability [5,6]. In addition, transition metal oxides have been considered as electrode materials in various electrochemical devices due to their high electrical conductivity and rich redox activity compared with the two corresponding single-component oxides [7]. In general, ruthenium oxide has been used as electrode material in pseudocapacitors due to its high theoretical capacitance [8]. However, its high cost and low conductivity prevent the extensive use of ruthenium oxide as an electrode in supercapacitors. Therefore, manganese oxide [9–15], nickel oxide [9,16,17], and iron oxide [18,19] have been considered as alternative electrode materials due to their low cost, natural abundance, and environmental advantage [20]. Among them, manganese oxide exhibits superior electrochemical performance, mediated via reversible oxygen reduction [21]. However, the commercialization of the manganese oxide electrode is limited by several issues, such as a low specific surface area, poor electrical conductivity, and unstable performance due to structural transition [8]. Perovskite oxide with a mixed transition metal could be an alternative because of its structural stability and high electrical conductivity [22].

A perovskite structure with the general formula of ABO_3 (the A site is a rare and alkaline earth metal cation, and the B -site is a 3d transition metal cation) has been extensively explored due to its high redox and thermal stability, high oxygen storage capacity, structural stability at high temperature, and inherent ability to carry oxygen vacancy [23,24]. Therefore, the perovskite structure has been used in various fields, such as electrochemical sensors [25], solar cells [26], fuel cells [27], and metal-ion batteries [28]. The electrode material used in supercapacitors needs to have a high specific surface area as well as excellent catalytic properties. However, the perovskite oxides synthesized via solid-state reactions and sol-gel methods exhibit low specific surface areas due to a high calcination temperature of 1073–1173 K, inducing particle agglomeration [29–31]. In recent years, several research groups have reported that transition metal oxides containing small particle sizes and high specific areas can be fabricated via low-temperature heat treatment, resulting in excellent electrochemical properties and structural stability [32–34]. Crystalline particles with high purity and uniform crystal size can be obtained via hydrothermal synthesis. The hydrothermal synthesis method can obtain uniform nanoparticles at low crystallization temperature and calcination temperature compared to the sol-gel method. Hydrothermal synthesis at 773 K is known to restrict particle agglomeration. The composition, size, and morphology of crystalline particles and their distribution can be altered by changing experimental variables such as reaction time and temperature, the solvent, and the reaction pH [35–38].

In this study, $NiMnO_3$ was prepared via hydrothermal synthesis under different reaction times. The prepared perovskite $NiMnO_3$ oxide exhibited three-dimensional hierarchical morphology with an improved specific surface area and structural stability compared with the powder sample. It can be used as an active electrode material for supercapacitors and electrochemical catalysts.

2. Materials and Methods

2.1. Materials

Nickel (II) acetate tetrahydrate ($Ni(OCOCH_3)_2 \cdot 4H_2O$, 99.99%, Sigma Aldrich), manganese (II) acetate tetrahydrate ($((CH_3COO)_2Mn \cdot 4H_2O)$, 99.99%, Sigma Aldrich), and Urea (NH_2CONH_2 , 98%, Sigma Aldrich).

2.2. Synthesis of Three-Dimensional $NiMnO_3$ via Hydrothermal Method

Three-dimensional hierarchical structures with cubic $NiMnO_3$ were synthesized via a hydrothermal reaction by adding 10 mmol $Ni(OCOCH_3)_2 \cdot 4H_2O$ and 1.6 mmol $(CH_3COO)_2Mn \cdot 4H_2O$ to 30 mL distilled water. The solution was subjected to ultrasonic treatment for 1 h, followed by the addition of urea and stirring for 3 h. The solution was transferred into a Teflon-lined autoclave and

heated at 433 K for 4, 5, 6, and 8 h, respectively. Hydrothermal synthesis proceeded with the reaction time as a variable, and the autoclave was cooled down to room temperature. Three-dimensional hierarchical structures with a cube of NiMnO₃ were obtained after repeated washing with distilled water and ethanol. The product was dried overnight at 374 K in a vacuum oven and calcined at 773 K for 4 h in the air. The sample names were designated as NMO-4, NMO-5, NMO-6, and NMO-8, corresponding to the hydrothermal synthesis reaction times of 4, 5, 6, and 8 h, respectively.

2.3. Characterization

The crystal structure of the obtained sample was analyzed by X-ray diffraction (MiniFlex 600) with Cu K α radiation ($\lambda = 1.5406 \text{ \AA}$) in the 2θ range of 20° to 80° at $4^\circ/\text{min}$ by using Si powder as a standard internal material. The morphology of the obtained sample was analyzed by scanning electron microscopy and N₂ adsorption/desorption isotherms determined the specific surface area and pore size distribution of the samples at 77 K, using by Brunauer–Emmett–Teller (BET, BELSORP-mini II). The sample oxidation was determined via X-ray photoelectron spectroscopy (XPS, on a Thermo ESCALAB 250), using Al K α radiation. Electrochemical measurements were carried out on a BCS-815 electrochemical workstation. The RRDE-3A electrochemical workstation (RRDE) was used to electrochemically evaluate the oxygen reduction reaction (ORR).

2.4. Electrochemical Measurement

In the RRDE, cyclic voltammetry (CV) and linear sweep voltammetry (LSV) measurements were performed between -0.8 and -0.2 V at a scan rate of 10 mV s^{-1} in an O₂-saturated 0.1 M KOH solution. Before measurement, it was saturated with N₂ or O₂ for 20 min. Hg/HgO (1 M NaOH) was used as the reference electrode and a Pt foil as the counter electrode. The area of each electrode was about 1 cm^2 and a 6 M KOH aqueous solution was used as an electrolyte. The electrochemical measurements were performed using the working electrode fabricated by mixing 80 wt.% of electrode material, 10 wt.% of binder (PVDF), 10 wt.% of Super-P as conductive carbon material, and N-methyl-2-pyrrolidone as the solvent to yield a slurry. The slurry was pressed onto the nickel foam current collector and dried at 100°C in a vacuum oven for 1 h. The specific capacitance from galvanostatic charge discharge (GCD) was calculated using the following formula:

$$C = \frac{I\Delta t}{m\Delta V} \quad (1)$$

where C ($\text{F}\cdot\text{g}^{-1}$) denotes the specific capacitance, Δt (s) represents the discharge time, I (A) is the discharge current, ΔV (V) refers to voltage, and m (g) indicates the mass of electrode material.

3. Results and Discussion

3.1. Characterization of Samples

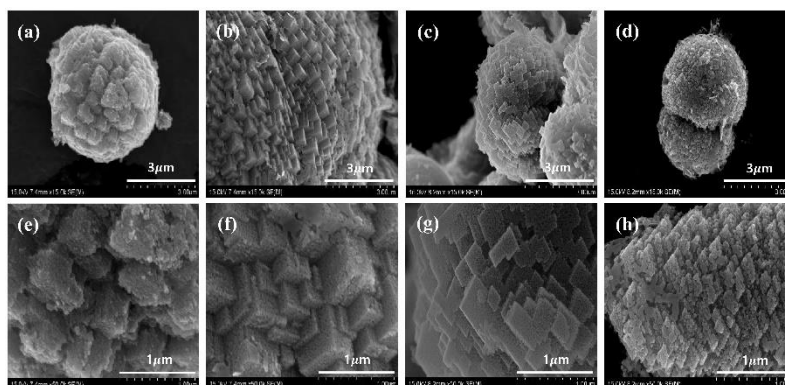


Figure 1. (a,e) SEM images of NMO-4; (b,f) NMO-5; (c,g) NMO-6 and (d,h) NMO-8.

Three-dimensional NiMnO₃ was prepared via one-step hydrothermal synthesis under various reaction times. Figure 1 shows the morphology of NiMnO₃ prepared by a one-step hydrothermal method with different reaction times. In general, the structural change induced by crystal growth can be explained using the Ostwald ripening mechanism [39]. Ostwald ripening is observed in a solid solution that describes the structural variation over time, the small particle agglomeration of a nanocube, and redeposition onto larger crystals. The NMO-4 sample revealed a limited three-dimensional hierarchical structure compared with other samples (Figure 1a,e). Compared with NMO-4, the size of the cube-like nanoparticles increased with hydrothermal synthesis reaction time. NMO-5 showed a three-dimensional hierarchical structure and the edge length of the cube was about 500 nm (Figure 1b,f). NMO-6 presented a smooth nanocube surface due to nanoparticle agglomeration (Figure 1c,g). When the reaction time was extended to 8 h, the nanocube was agglomerated and the hierarchical morphology was destroyed. The prepared NiMnO₃ morphology revealed a three-dimensional hierarchical structure, which affected the electrochemical performance of the supercapacitor due to its high specific surface area and stability compared with other general powder samples [8,40].

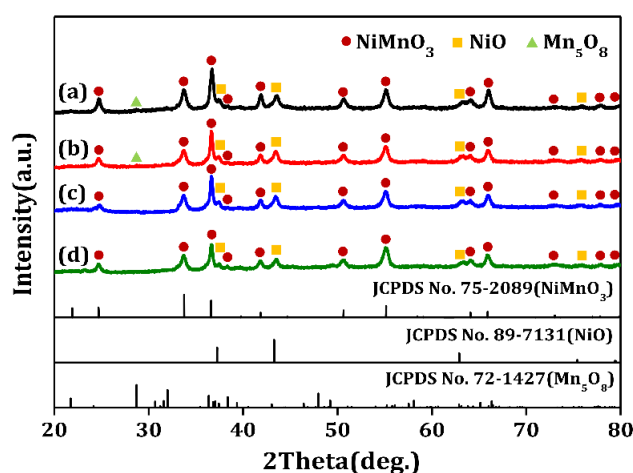


Figure 2. XRD pattern of (a) NMO-4; (b) NMO-5; (c) NMO-6 and (d) NMO-8.

X-ray diffraction studies revealed the crystal phase and structural properties of the prepared NiMnO₃. The XRD pattern of NiMnO₃ showed diffraction peaks similar to the perovskite oxide phase, which exhibited structural stability and conductivity, as shown in Figure 2. Additionally, all samples exhibited the NiMnO₃ phase (JCPDS No. 75-2089) and small impurity peaks, such as Mn₅O₈ (JCPDS No. 72-1427) and NiO (JCPDS No. 89-7131), along with diffraction peaks of NiMnO₃. Diffraction peaks of impurity appeared due to a less-formed solid phase as the reaction time decreased. As can be seen in Figure 2a,b, the diffraction peak of Mn₅O₈ disappeared when the hydrothermal synthesis reaction time was longer than 6 h. Transition metal oxides should have low impurity that induces low charge mobility and electroconductivity [41]. The other diffraction peaks of impurity diminished as the reaction time increased over 6 h. Compared with other samples, NMO-8 exhibited a lower peak intensity, as shown in Figure 2d, which may be attributed to the low level of crystallization related to redeposition onto larger crystals [41].

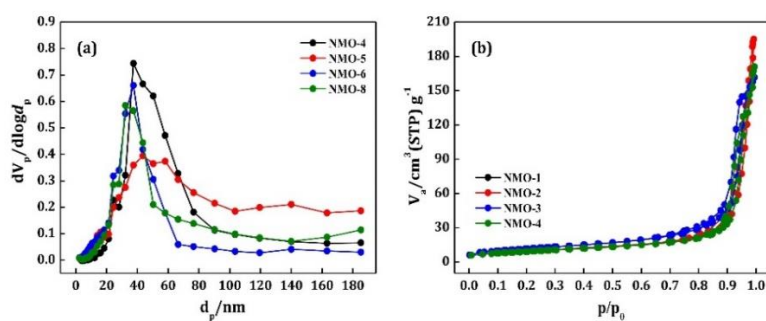


Figure 3. (a) Pore size distribution; (b) the nitrogen adsorption-desorption isotherms of NiMnO₃.

Table 1. The specific surface areas calculated by the Brunauer–Emmett–Teller (BET) method.

Sample	Surface Area (m ² ·g ⁻¹)	Pore Volume (mL·g ⁻¹)	Average Pore Diameter (nm)
NMO-4	32.036	0.2821	36.361
NMO-5	33.301	0.2693	33.881
NMO-6	40.821	0.2445	23.956
NMO-8	32.645	0.2440	29.899

Figure 3 shows the specific surface area, pore volume, and size distribution of NiMnO₃ via one-step hydrothermal synthesis with different synthesis times. The supercapacitor electrode materials require a high specific surface area, which is related to the large active surface area and electrochemical double layer. The duration of synthesis affected the crystal morphology as well as the specific surface area. The specific surface area of NMO-6 was 40.821 m²·g⁻¹ and was higher than the other samples (Table 1 and Figure 3b). The large surface area of NMO-6 associated with particle size or morphology was controlled by hydrothermal synthesis at low temperatures. The specific surface area of the NMO-8 sample decreased due to the agglomeration of nanocube morphology, as shown in Figure 1d,h. The dense nanocubes in the three-dimensional hierarchical structure reduced the pore diameter and increased the surface area (Table 1). A high specific surface reduced the overpotential of ORR via the accelerated mass transfer of reactants and reaction products [42], increasing the stability of the material for efficient charge transport and enhanced ORR electrochemical catalytic activity.

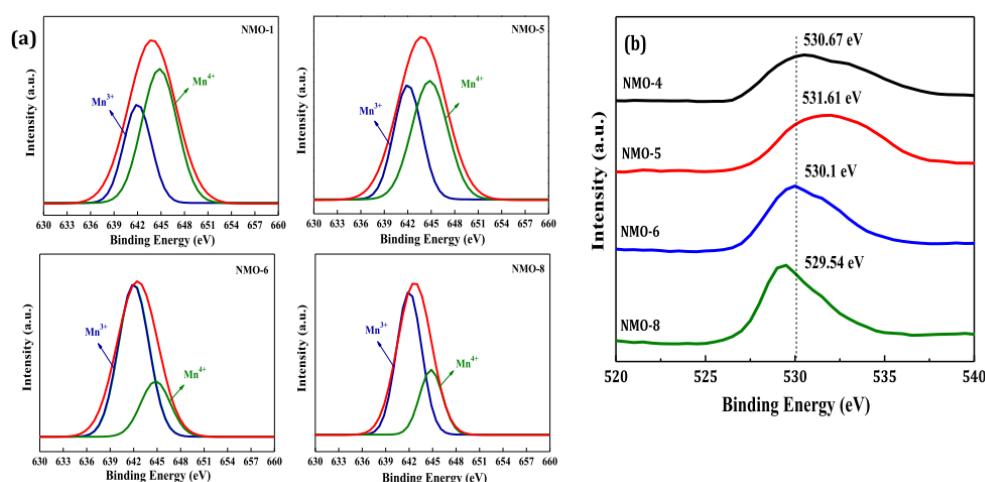


Figure 4. (a) Mn 2p^{3/2} spectra; (b) O 1s spectra of NiMnO₃ via hydrothermal synthesis at 433 K.

In the perovskite structure, manganese oxidation in the *B*-site is relevant to the lack of oxygen ion and the oxygen vacancy. In NiMn(IV)O_3 , a transition from Mn^{4+} to Mn^{3+} of manganese oxidation in the *B*-site decreases the number of oxygen ions in order to achieve electrical neutrality. As a result, an oxygen vacancy is formed, which affects electroconductivity and pseudocapacitance due to the charge transfer. In order to confirm the oxidation state of manganese, X-ray photoelectron spectroscopy was performed and Figure 4a shows the XPS spectra of Mn $2p^{3/2}$. The area ratios of the $\text{Mn}^{3+}/\text{Mn}^{4+}$ spectra of NMO-4, NMO-5, NMO-6, and NMO-8 were 0.711, 0.867, 1.575, and 1.342, respectively. NMO-6 showed a higher ratio of Mn^{3+} than the other prepared samples. The higher ratio of Mn^{3+} in NMO-6 indicates that the reduction of the Mn_5O_8 oxide caused the manganese oxidation number to reduce to Mn^{3+} in the perovskite NiMnO_3 oxide by increasing the reaction time to 6 h. The ratio of $\text{Mn}^{3+}/\text{Mn}^{4+}$, depending on the reaction period, and the high ratio of Mn^{3+} improved electroconductivity due to oxygen vacancy [23,43,44]. Figure 4b shows that the O 1s spectra of NMO-8 shifted to lower binding energy than other samples and the peak width was narrower compared with other samples due to the reduced crystallization of NMO-8 [41].

3.2. Oxygen Reduction Reaction (ORR) Activity

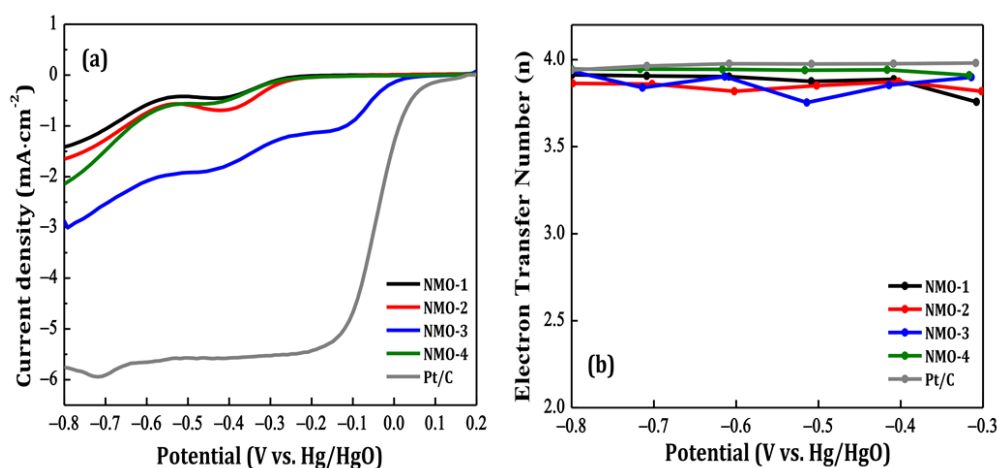


Figure 5. (a) Linear sweep voltammogram (LSV) curves for oxygen reduction reaction (ORR) polarization curves of NiMnO_3 obtained by the RRDE-3A electrochemical workstation (RRDE) in O_2 -saturated 0.1 M KOH; (b) Electron transfer number of the NiMnO_3 .

RRDE experiments were conducted to identify the performance of the perovskite oxide as ORR electrochemical catalytic material. Because the commercial ORR catalyst, Pt/C, is expensive, cost-effective perovskite oxide was considered as an ORR electrochemical catalyst in this study. Perovskite oxide is a good electrochemical catalyst for energy conversion and storage devices as it enhances the movement of oxygen ions through the oxygen vacancies [45]. The electrochemical catalytic activity is determined by the *B*-site transition metal in the perovskite structure [46]. The diffusion of oxygen vacancy or cation in the transition metal oxide affects ORR catalytic activity due to changes in the lattice and electronic structures. The high specific surface area and oxygen vacancy improve the conductivity and ORR catalytic activity due to multiple catalytic active sites on the surface. Despite the difference in onset potential compared with commercial catalysts such as Pt/C, NMO-6 exhibited higher electrocatalytic activity compared with other samples due to high specific surface area and oxygen vacancy (Figure 5a). The transition state of the Mn in the *B*-site of NiMnO_3 from Mn^{4+} to Mn^{3+} increased the active site on the surface, conductivity, and the catalytic activity of the electrode material due to the oxygen vacancies generated. NMO-6 samples with a high ratio of Mn^{3+} in the *B*-site had high ORR catalytic activity compared to other samples because the higher Mn^{3+} caused many oxygen vacancies to satisfy the electrical neutrality. Oxygen vacancies can provide multiple catalytic active sites. Therefore, NMO-6 exhibited higher catalytic activity than other samples. The ORR catalyst also exhibited high current density at the same potential state. To confirm this finding, the

potential of each sample was compared at a constant current. As a result, NMO-6 displayed higher potential state than the other prepared samples. ORR can proceed by a two-electron pathway or a four-electron pathway [47]. The two-electron reaction is associated with a low conversion efficiency due to hydrogen peroxide as a by-product, which damages the electrolyte membrane. Therefore, the four-electron reactions are preferred by the ORR catalyst. Compared with the commercial catalyst Pt/C, the prepared NiMnO₃ underwent a close four-electron reaction (Figure 5b). A diffusion-limited current region of the Pt/C was observed under -0.2 V. While the prepared NiMnO₃ had good ORR catalytic activity and the number of reaction electron numbers was close to four, the diffusion-limited current region of NiMnO₃ was not clearly detected due to the poor reaction rate.

3.3. Supercapacitor Performance

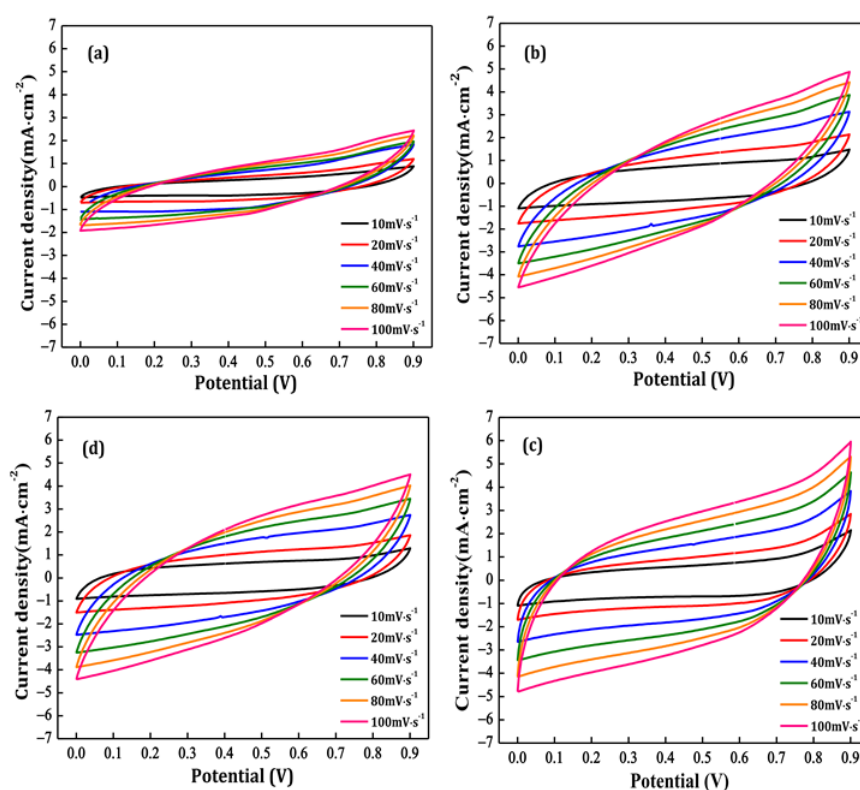


Figure 6. (a) Cyclic voltammograms of NMO-4; (b) NMO-5; (c) NMO-6; (d) NMO-8 electrode at various scan rates (10–100 $\text{mV}\cdot\text{s}^{-1}$) in 6 M KOH.

The electrochemical performance of the prepared NiMnO₃ was investigated via cyclic voltammogram (CV) and galvanostatic charge–discharge measurements using 6.0 M KOH. Figure 6 shows the CV curves of the symmetric supercapacitor device at scan rates from 10 to 100 $\text{mV}\cdot\text{s}^{-1}$. All samples displayed nearly-rectangular and asymmetric CV curves, indicating a fast ion diffusion rate and a low internal resistance of the device. In addition, even at a high scan rate, all supercapacitors exhibited the nearly rectangular and asymmetric CV curves, indicating that the perovskite electrode materials have pseudocapacitive properties [48]. As shown in Figure 7a, NMO-6 showed a high specific capacitance of $99.03 \text{ F}\cdot\text{g}^{-1}$, which is attributed to the reduction in diffusion distance by well-developed mesoporous and a larger active catalytic surface area due to the high specific surface area. To evaluate the electrochemical performance of the NiMnO₃ electrode at a high current density, constant charge/discharge experiments were conducted at the current densities of 1, 3, 5, and 7 $\text{mA}\cdot\text{cm}^{-2}$ in the voltage range of 0–0.9 V under 6.0 M KOH electrolyte. The higher current density restricts electrolyte ion movement and decreases specific capacitance [49]. As shown in Figure 7b, the specific capacitance at 1 $\text{mA}\cdot\text{cm}^{-2}$ was higher compared with the other current densities because the

electrolyte ion diffusion occurs easily at a low current density. Figure 7c shows that the NiMnO₃ electrode after 7000 charge/discharge cycle tests at a current density of 1 mA·cm⁻² had 77% specific capacitance compared with the initial capacitance. Despite the charge storage of the supercapacitor electrode via redox reaction, continuous redox reaction leads to the loss of the transition metal oxide, which can reduce the electrochemical properties [50].

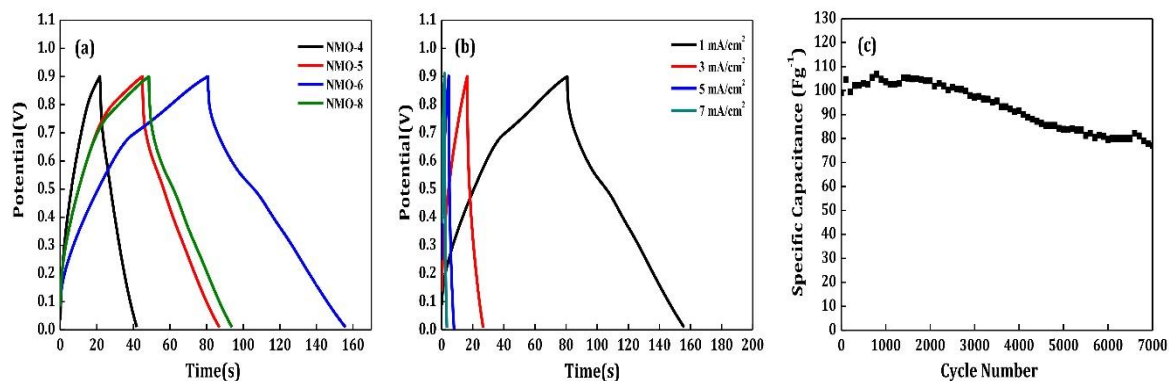


Figure 7. (a) Electrochemical performance of NiMnO₃ electrode material with different reaction times; (b) galvanostatic charge discharge (GCD) curve of NMO-6 at different currents; (c) cycling performance of NiMnO₃ at 1 mA·cm⁻² current density.

5. Conclusions

A nanocube-like NiMnO₃ perovskite oxide was fabricated using the hydrothermal method by simply adjusting the reaction time. NMO-6, which was prepared via hydrothermal synthesis for 6 hours, showed superior specific capacitance compared with other samples due to the larger specific surface area and the increased ratio of Mn³⁺ and oxygen vacancy. The enhanced electrochemical performance showed excellent cycle stability with a coulombic efficiency of 77% even after 7000 cycles. The performance was relevant to the increase of the active site due to the three-dimensional structure of the sample and the well-developed mesopore, which reduced the diffusion distance of the electrolyte ion. Based on the results, the fabricated NiMnO₃ perovskite oxide can be used as an active electrode material in supercapacitors and electrochemical catalysts.

Author Contributions: conceptualization, I.C. and Y.W.; methodology, Y.W.; validation, H.Y., J.Y. and Y.W.; investigation, H.Y.; data curation, H.Y.; writing—original draft preparation, H.Y.; writing—review and editing, J.Y. and Y.W.; visualization, H.Y.; supervision, I.C. and Y.W. All authors have read and agreed to the published version of the manuscript.

Funding: This research was supported by Basic Science Research Program through the National Research Foundation of Korea (NRF) funded by the Ministry of Education (NRF-2016R1D1A1B03931239), research and development program of the Korea Institute of Energy Research (B9-5506), which is granted financial resources from Gwangju metropolitan city, Republic of Korea. This work was supported by the Basic Science Research Program through the National Research Foundation of Korea (NRF) funded by the Ministry of Education (NRF-2018R1D1A1A02085324).

Conflicts of Interest: The authors declare no conflict of interest.

References

1. Libich, J.; Máca, J.; Vondrák, J.; Čech, O.; Sedlaříková, M. Supercapacitors: Properties and applications. *J. Energy Storage* **2018**, *17*, 224–227.
2. Raza, W.; Ali, F.; Raza, N.; Luo, Y.; Kim, K.H.; Yang, J.; Kumar, S.; Mehmood, A.; Kwon, E.E. Recent advancements in supercapacitor technology. *Nano Energy* **2018**, *52*, 441–473.
3. Yan, X.; You, H.; Liu, W.; Wang, X.; Wu, D. Free-Standing and Heteroatoms-Doped Carbon Nanofiber Networks as a Binder-Free Flexible Electrode for High-Performance Supercapacitors. *Nanomaterials* **2019**, *9*, 1189.

4. Qiao, S.; Huang, N.; Zhang, J.; Zhang, Y.; Sun, Y.; Gao, Z. Microwave-assisted synthesis of Fe-doped NiMnO₃ as electrode material for high-performance supercapacitors. *J. Solid State Electrochem.* **2019**, *23*, 63–72.
5. Wei, H.; Wang, J.; Yu, L.; Zhang, Y.; Hou, D.; Li, T. Hydrothermal preparation of nickel-manganese oxide with microsphere structure grown on Ni foam and supercapacitive performance. *Mater. Lett.*, **2017**, *187*, 11–14.
6. Tian, D.; Lu, X.; Nie, G.; Gao, M.; Wang, C. Direct growth of Ni–Mn–O nanosheets on flexible electrospun carbon nanofibers for high performance supercapacitor applications. *Inorg. Chem. Front.* **2017**, *5*, 635–642.
7. Hwang, H.Y.; Iwasa, Y.; Kawasaki, M.; Keimer, B.; Nagaosa, N.; Tokura, Y. Emergent phenomena at oxide interfaces. *Nat. Mater.* **2012**, *11*, 103–113.
8. Kakaei, K.; Esrafil, M.D.; Ehsani, A. Alcohol Oxidation and Hydrogen Evolution. *Interface Sci. Technol.* **2019**, *27*, 253–301.
9. Brousse, T.; Bélanger, D. A Hybrid Fe₃O₄-MnO₂ Capacitor in Mild Aqueous Electrolyte. *Electrochem. Solid-State Lett.* **2003**, *6*, A244–A248.
10. Bodoardo, S.; Penazzi, N.; Spinelli, P.; Arrabito, M. Influence of aluminium doping on the electrochemical behaviour of manganese dioxide. *J. Power Sources* **2001**, *94*, 194–200.
11. Shinomiya, T. Gupta, V.; Miura, N. Effects of electrochemical-deposition method and microstructure on the capacitive characteristics of nano-sized manganese oxide. *Electrochim. Acta* **2006**, *51*, 4412–4419.
12. Hu, C.C.; Tsou, T.W. Capacitive and textural characteristics of hydrous manganese oxide prepared by anodic deposition. *Electrochim. Acta* **2002**, *47*, 3523–3532.
13. Broughton, J.N.; Brett, M.J. Variations in MnO₂ electrodeposition for electrochemical capacitors. *Electrochim. Acta* **2005**, *50*, 4814–4819.
14. Chang, J.K.; Chen, Y.L.; Tsai, W.T. Effect of heat treatment on material characteristics and pseudo-capacitive properties of manganese oxide prepared by anodic deposition. *J. Power Sources* **2004**, *135*, 344–353.
15. Prasad, K.R.; Miura, N. Potentiodynamically deposited nanostructured manganese dioxide as electrode material for electrochemical redox supercapacitors. *J. Power Sources* **2004**, *135*, 354–360.
16. Wu, C.; Zhu, Y.; Ding, M.; Jia, C.; Zhang, K. Fabrication of plate-like MnO₂ with excellent cycle stability for supercapacitor electrodes. *Electrochim. Acta* **2018**, *291*, 249–255.
17. Lee, J.Y.; Liang, K.; An, K.H.; Lee, Y.H. Nickel oxide/carbon nanotubes nanocomposite for electrochemical capacitance. *Synth. Met.* **2005**, *150*, 153–157.
18. Yuan, C.; Zhang, X.; Wu, Q.; Gao, B. Effect of temperature on the hybrid supercapacitor based on NiO and activated carbon with alkaline polymer gel electrolyte. *Solid State Ion.* **2006**, *177*, 1237–1242.
19. Wu, N.L.; Wang, S.Y.; Han, C.Y.; Wu, D.S.; Shiue, L.R. Electrochemical capacitor of magnetite in aqueous electrolytes. *J. Power Sources* **2003**, *113*, 173–178.
20. Wu, N.L. Nanocrystalline oxide supercapacitors. *Mater. Chem. Phys.* **2002**, *75*, 6–11.
21. Liu, E.H.; Li, W.; Li, J.; Meng, X.Y.; Ding, R.; Tan, S.T. Preparation and characterization of nanostructured NiO/MnO₂ composite electrode for electrochemical supercapacitors. *Mater. Res. Bull.* **2009**, *44*, 1122–1126.
22. Kakvand, P.; Rahmanifar, M.S.; El-Kady, M.F.; Pendashteh, A.; Kiani, M.A.; Hashami, M.; Najafi, M.; Abbasi, A.; Mousavi, M.F.; Kaner, R.B. Synthesis of NiMnO₃/C nano-composite electrode materials for electrochemical capacitors. *Nanotechnology* **2016**, *27*, 315401.
23. Kim, C.; Gwon, O.; Jeon, I.Y.; Kim, Y.; Shin, J.; Ju, Y.W.; Baek, J.B.; Kim, G. Cloud-like graphene nanoplatelets on Nd_{0.5}Sr_{0.5}CoO_{3-δ} nanorods as an efficient bifunctional electrocatalyst for hybrid Li–air batteries. *J. Mater. Chem. A* **2016**, *4*, 2122–2127.
24. Han, Y.H. Defect Chemistry in Simple ATiO₃ Perovskite Ceramics. *Korean J. Mater. Res.* **1992**, *2*, 248–256.
25. Di Bartolomeo, E.; Kaabuuathong, N.; D’Epifanio, A.; Grilli, M.L.; Traversa, E.; Aono, H.; Sadaoka, Y. Nano-structured perovskite oxide electrodes for planar electrochemical sensors using tape casted YSZ layers. *J. Eur. Ceram. Soc.* **2004**, *24*, 1187–1190.
26. Tsvetkov, N.; Moon, B.C.; Lee, J.; Kang, J.K. Controlled synthesis of nanocrystalline Nb:SrTiO₃ electron transport layers for robust interfaces and stable high photovoltaic energy conversion efficiency in perovskite halide solar cells. *ACS Appl. Energy Mater.* **2019**, doi:10.1021/acsam.9b01592
27. Tao, S.; Irvine, J.T. Catalytic properties of the perovskite oxide La_{0.75}Sr_{0.25}Cr_{0.5}Fe_{0.5}O_{3-δ} in relation to its potential as a solid oxide fuel cell anode material. *Chem. Mater.* **2014**, *16*, 4116–4121.

28. Yue, B.; Hu, Q.; Ji, L.; Wang, Y.; Liu, J. Facile synthesis of perovskite CeMnO₃ nanofibers as an anode material for high performance lithium-ion batteries. *RSC Adv.* **2019**, *9*, 38271–38279.
29. Xiulan, C.; Yuan, L. New methods to prepare ultrafine particles of some perovskite-type oxides. *Chem. Eng. J.* **2000**, *78*, 205–209.
30. Tarancón, A.; Skinner, S.J.; Chater, R.J.; Hernández-Ramírez, F.; Kilner, J.A. Layered perovskites as promising cathodes for intermediate temperature solid oxide fuel cells. *J. Mater. Chem.* **2007**, *17*, 3175–3181.
31. Lim, C.; Kim, C.; Gwon, O.; Jeong, H.Y.; Song, H.K.; Ju, Y.W.; Shin, J.; Kim, G. Nano-perovskite oxide prepared via inverse microemulsion mediated synthesis for catalysis of lithium-air batteries. *Electrochim. Acta* **2018**, *275*, 248–255.
32. Kim, H.U.; Sun, Y.K.; Lee, B.S.; Jin, C.S.; Shin, K.H. Synthesis of defective-structure Li₄Mn₅O₁₂ by combustion method and its application to hybrid capacitor. *J. Korean Electrochem. Soc.* **2010**, *13*, 103–109.
33. Stein, A.; Keller, S.W.; Mallouk, T.E. Turning down the heat: Design and mechanism in solid-state synthesis. *Science* **1993**, *259*, 1558–1564.
34. Zawadzki, M.; Wrzyszczyk, J. Hydrothermal synthesis of nanoporous zinc aluminate with high surface area. *Mater. Res. Bull.* **2000**, *35*, 109–114.
35. Cho, C.W.; Tai, W.P.; Lee, H.S. Characteristics of Zirconia Nanoparticles with Hydrothermal Synthesis Process. *J. Korean Ind. Eng. Chem.* **2014**, *25*, 564–569.
36. Feng, S.; Xu, R. New materials in hydrothermal synthesis. *Acc. Chem. Res.* **2001**, *34*, 239–247.
37. Cai, D.; Liu, B.; Wang, D.; Liu, Y.; Wang, L.; Li, H.; Wang, Y.; Wang, C.; Li, Q.; Wang, T. Facile hydrothermal synthesis of hierarchical ultrathin mesoporous NiMoO₄ nanosheets for high performance supercapacitors. *Electrochim. Acta* **2014**, *115*, 358–363.
38. Ni, J.; Gao, J.; Wei, H.; Geng, X. Controlled hydrothermal synthesis and excellent optical properties of two different kinds of CeO₂ nanocubes. *J. Mater. Sci. Mater. Electron.* **2017**, *28*, 11029–11033.
39. Lin, M.; Fu, Z.Y.; Tan, H.R.; Tan, J.P.Y.; Ng, S.C.; Teo, E. Hydrothermal synthesis of CeO₂ nanocrystals: Ostwald ripening or oriented attachment? *Cryst. Growth Des.* **2012**, *12*, 3296–3303.
40. Conway, B.E. *Electrochemical Supercapacitors: Scientific Fundamentals and Technological Applications*; Springer Science & Business Media: Berlin, Germany, 2013.
41. Oh, T. Correlation between oxygen related bonds and defects formation in ZnO thin films by using X-ray diffraction and X-ray photoelectron spectroscopy. *Korean J. Mater. Res.* **2013**, *23*, 580–585.
42. Osgood, H.; Devaguptapu, S.V.; Xu, H.; Cho, J.; Wu, G. Transition metal (Fe, Co, Ni, and Mn) oxides for oxygen reduction and evolution bifunctional catalysts in alkaline media. *Nano Today* **2016**, *11*, 601–625.
43. Pech, D.; Brunet, M.; Durou, H.; Huang, P.; Mochalin, V.; Gogotsi, Y.; Taberna, P.L.; Simon, P. Ultrahigh-power micrometre-sized supercapacitors based on onion-like carbon. *Nat. Nanotechnol.* **2010**, *5*, 651–654.
44. Simon, P.; Gogotsi, Y. Materials for electrochemical capacitors. In *Nanoscience And Technology: A Collection of Reviews from Nature Journals*; Emerald Group Publishing Limited: Bingley, UK, 2010; pp. 320–329.
45. Chen, C.F.; King, G.; Dickerson, R.M.; Papin, P.A.; Gupta, S.; Kellogg, W.R.; Wu, G. Oxygen-deficient BaTiO_{3-x} perovskite as an efficient bifunctional oxygen electrocatalyst. *Nano Energy* **2015**, *13*, 423–432.
46. Sunarso, J.; Torriero, A.A.; Zhou, W.; Howlett, P.C.; Forsyth, M. Oxygen reduction reaction activity of La-based perovskite oxides in alkaline medium: A thin-film rotating ring-disk electrode study. *J. Phys. Chem. C* **2012**, *116*, 5827–5834.
47. Khan, I.A.; Qian, Y.; Badshah, A.; Nadeem, M.A.; Zhao, D. Highly porous carbon derived from MOF-5 as a support of ORR electrocatalysts for fuel cells. *ACS Appl. Mater. Interfaces* **2016**, *8*, 17268–17275.
48. Mefford, J.T.; Hardin, W.G.; Dai, S.; Johnston, K. P.; Stevenson, K.J. Anion charge storage through oxygen intercalation in LaMnO₃ perovskite pseudocapacitor electrodes. *Nat. Mater.* **2014**, *13*, 726–732.
49. Chen, N.; Ni, L.; Zhou, J.; Zhu, G.; Kang, Q.; Zhang, Y.; Chen, S.; Zhou, W.; Lu, C.; Chen, J.; et al. Sandwich-like holey graphene/PANI/graphene nanohybrid for ultrahigh-rate supercapacitor. *ACS Appl. Energy Mater.* **2018**, *1*, 5189–5197.
50. Oh, I.; Kim, M.; Kim, J. Hollow Carbon/FeOOH Nanocomposites for Supercapacitor Application. *Polym. Korea* **2016**, *40*, 26–32.

